


PAPER

[View Article Online](#)
[View Journal](#) | [View Issue](#)Cite this: *J. Mater. Chem. A*, 2020, **8**, 17163

Reduced energy loss in SnO₂/ZnO bilayer electron transport layer-based perovskite solar cells for achieving high efficiencies in outdoor/indoor environments†

Young Wook Noh,[‡] In Su Jin,[‡] Kyeong Su Kim, Sang Hyun Park and Jae Woong Jung *

The energy loss in perovskite solar cells (PSCs) is a key factor that limits the full potential of photovoltaic performance to values below the Shockley–Queisser limit. Herein, we report a bilayer structure of the electron transport layer (ETL) for reducing energy loss in methylammonium lead triiodide (MAPbI₃)-based planar heterojunction PSCs. The controlled electronic structure of the bilayer ETL affords suitable energy band matching at the interface of the MAPbI₃ layer for electron transport/hole blocking, which effectively suppresses trap-assisted recombination at the interface of PSCs. As a result, the optimized bilayer ETL reduces charge recombination at the interfaces of the perovskite layer, boosting the power conversion efficiency (PCE) of the MAPbI₃-based PSCs up to 20.43% with an open circuit voltage (V_{OC}) as high as 1.20 V under 1 sun conditions. In addition, the bilayer ETL-based devices retained a high V_{OC} of 0.98 V under illumination from a white light emitting diode (1000 lux), realizing PCEs of up to 37.2% under indoor conditions with good ambient stability for >800 h. These findings suggest the importance and potential of the bilayer ETL for reduced energy loss to generate high power outputs in outdoor/indoor environments of PSCs.

Received 6th May 2020
Accepted 22nd July 2020

DOI: 10.1039/d0ta04721j

rsc.li/materials-a

1. Introduction

Organic–inorganic hybrid metal halide perovskites have been revolutionized in the past few years, providing new prospects of high efficiency photovoltaic technology at low cost.^{1–9} The power conversion efficiencies (PCEs) of perovskite solar cells (PSCs) have been competing with those of typical photovoltaic technologies such as polycrystalline or amorphous silicon as the PCE of single-junction PSCs exceeds 25% in single-junction devices.¹⁰ However, it is still far from the theoretical Shockley–Queisser limit (SQL), which is ~30.5% PCE for a single-junction cell based on methylammonium lead triiodide (MAPbI₃).^{11–13} In particular, the short-circuit current density (J_{SC}) and fill factor (FF) of PSCs are approaching the SQL, while the open-circuit voltage (V_{OC}) is far below the radiative limit and internal V_{OC} s (~1.32 V and ~1.28 V in the case of MAPbI₃, respectively) mainly due to the non-radiative recombination losses.^{14,15} Thus, it is desirable to minimize the non-radiative recombination pathways in the bulk and at the interfaces toward efficient charge

carrier extraction to further improve the photovoltaic performance of PSCs.

Enormous effort has been dedicated to reduce the energy loss of PSCs through modified crystallization, surface passivation, doping, and composition engineering of the perovskite layer. The recent progress of bulk (*e.g.*, metal doping or using a non-stoichiometric ratio of PbI₂) or surface engineering in MAPbI₃ films boosted the V_{OC} s well over 1.20 V in single-junction devices, so the control of trap density inside the bulk MAPbI₃ or its surface contributes to reduced energy loss and enhanced PCEs of PSCs.^{16–21} In addition to engineering of the perovskite layer, the formation of appropriate charge-selective contact is another key strategy in determining the device properties because the photo-generated carriers should pass through the interfaces before arriving at the electrodes. The optimal interfacial contact not only forms an ideal energy-level alignment for each layer in the device but also provides appropriate physical properties at the interfaces, and thus it governs the trap density in planar heterojunction PSCs.^{22–24} Besides the typical electron transport layer such as tin dioxide (SnO₂) or titanium dioxide (TiO₂), enormous effort has been devoted to developing new ETL materials, such as Zn₂SnO₄ and In₂O₃.^{25,26} However, novel ETL materials with impressive PCEs have been rarely reported, and their V_{OC} s were still below the theoretical limits. For example, Seok and co-workers reported

Department of Advanced Materials Engineering for Information & Electronics, Kyung Hee University, 1732 Deogyong-daero, Giheung-gu, Yongin-si, Gyeonggi-do 446-701, Republic of Korea. E-mail: wodndwj@khu.ac.kr

† Electronic supplementary information (ESI) available. See DOI: 10.1039/d0ta04721j

‡ These authors contributed equally to this work.

PCEs as high as 21.3% in MAPbI₃-based PSCs when using BaSnO₃ as an ETL material, but V_{OC} remained at 1.12 V.²⁷ Given that the reduced V_{OC} from the theoretical maximum is due to non-radiative charge recombination present in the un-optimized interfaces, there is still great potential to further tune the interfacial properties for efficient charge transport and suppressed energy loss.

To overcome these challenges, we design a bilayer structure of SnO₂/ZnO as a promising ETL for MAPbI₃-based PSCs. The insertion of ZnO between ITO and SnO₂ allows more well-matched energy levels and an efficient electron transport ability, so the ETL forms more favorable energy level alignment and charge transport channels than the single ETL of SnO₂. The electronic properties of the bilayer ETL were optimized by varying thermal treatment on the bottom ZnO layer, and the non-annealed one exhibited more favorable features including superior film quality, better band alignment, suppressed trap density, and reduced charge recombination. As a result, the bilayer ETL achieves PCEs as high as 20.43% with a V_{OC} of 1.20 V in the single junction MAPbI₃-based PSCs under 1 sun illumination (100 mW cm⁻²). More importantly, the suppressed non-radiative energy loss in the optimized bilayer ETL retained a high V_{OC} of 0.98 V under white light emitting diode (LED) light (6500 K, 1000 lux), achieving a record PCE of 37.2%. The bilayer ETL-based device also exhibited long-term stability (>800 h) under ambient conditions and continuous LED light illumination. This work paves a way to realize efficient and practical PSCs with high ambient stability that are potentially applicable in power generation in outdoor/indoor environments.

2. Experimental section

2.1. Materials

The precursor solution of ZnO was prepared by dissolving 80 mg of ZnO NPs (Sigma Aldrich, nanopowder < 100 nm) in 12 ml of aqueous ammonium hydroxide solution (28%). The perovskite precursor solution was prepared by dissolving PbI₂ (perovskite grade, TCI) (461 mg), CH₃NH₃I (perovskite grade, TCI) (159 mg), and anhydrous dimethyl sulfoxide (71 μ l) in anhydrous *N,N*-dimethylformamide (0.63 ml). The solution of hole transport layer was prepared by dissolving spiro-OMeTAD (Derthon) in chlorobenzene (20 mg ml⁻¹) with 23 μ l of bis(trifluoromethane) sulfonamide lithium salt in acetonitrile (90.9 mg ml⁻¹) and 39 μ l of 4-*tert*-butylpyridine (*t*BP).

2.2. Fabrication of thin-film perovskite solar cells

The indium tin oxide (ITO)-coated glass substrates were sequentially cleaned with water, acetone, and isopropanol under sonication for 30 min, and then the substrates were treated with UV-O₃ for 30 min. After the ZnO layer was formed by spin-coating onto the ITO-coated glass (3000 rpm for 30 s), the substrate was annealed in the ambient atmosphere for 1 h at 100 °C. After the substrates were cooled to RT, the electron transport layer was formed by spin-coating an aqueous dispersion of SnO₂ nanoparticles (Alfa) at 3000 rpm for 30 s. After the substrates were annealed in the ambient atmosphere for 1 h at

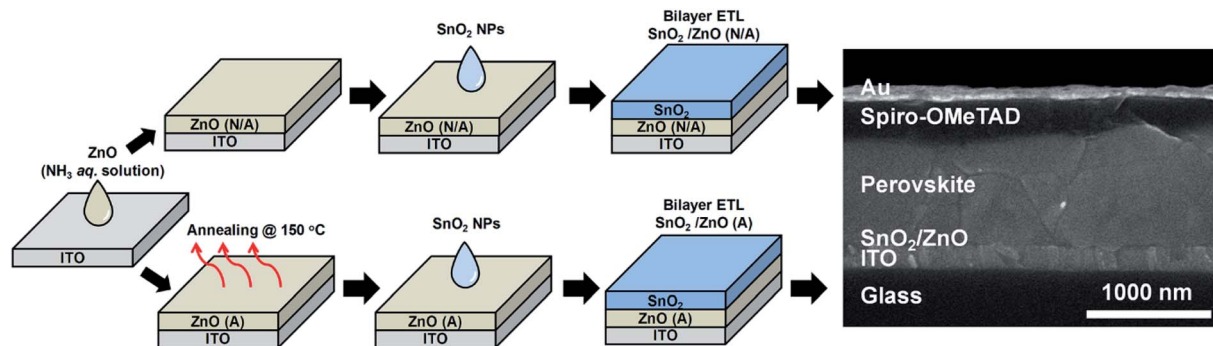
100 °C, the perovskite layer was formed by spin-coating the precursor solution at 1000 rpm for 10 s and 3000 rpm for 20 s, while 400 μ l of anhydrous diethyl ether was dripped on top of the substrates after 14 s of spinning. The dark-brown films were thermally annealed at 100 °C for 3 min, and then spiro-OMeTAD was deposited by spin-coating at 2000 rpm for 25 s. Finally, 80 nm of Au was evaporated under high vacuum (<5 \times 10⁻⁶ Torr). The active area was defined by a shadow mask to be 10 mm².

2.3. Characterization

Photoelectron spectroscopy was carried out using an X-ray photoelectron spectrometer (K Alpha, Thermo Science) and ultraviolet photoelectron spectrometer (AXIS Ultra DLD, Kratos Inc.) equipped with a He I source ($h\nu$ = 21.2 eV) at the Korea Basic Science Institute. Absorption and transmittance measurements were carried out using a spectrometer (Cary 100, Agilent). The fluorescence of the sample was measured using a spectrofluorometer (FS5, Edinburgh Instruments). The photoluminescence decay was monitored using a time-correlated single photon counting system using a picosecond laser with excitation at 405 nm. The thin film morphology was observed using an atomic force microscope (CoreAFM, Nanosurf) in tapping mode and a field-emission scanning electron microscope (S-4800, Hitachi). The photovoltaic performance of PSCs was obtained using a parameter analyzer (4200-SCS, Keithley) under AM 1.5G (100 mW cm⁻²) illumination in which the light intensity was carefully calibrated using an NREL-certified photodiode. In the case of the indoor conditions, a white light emitting diode lamp (6500 K) was applied as a light source, and the light intensity was calibrated to 500 and 1000 lux using a spectrometer (Spectrolux, GL Optic). The incident power of the light source was integrated from the spectrum (ESI[†]). The external quantum efficiency (EQE) of the device was measured using a lock-in amplifier system which records the short-circuit current density under chopped monochromatic light. Electrochemical impedance spectroscopy of the devices was investigated using a potentiostat (Compactstat, IVIUM). Intensity-modulated photovoltage spectroscopy (IMVS) and photocurrent spectroscopy (IMPS) were performed using a potentiostat with a light emitting diode (LED) system (IVIUM, IM1225).

3. Results and discussion

The bilayer ETL was prepared by depositing ZnO and SnO₂ layers sequentially onto the ITO-coated glass, as illustrated in Scheme 1. Two bilayer ETLs with different ZnO layers (thermally annealed and non-annealed ZnO denoted as ZnO (A) and ZnO (N/A) hereafter, respectively) were prepared to optimize the photovoltaic properties of the bilayer ETL-based PSCs. The bilayer structure is a robust ETL for growing a thick MAPbI₃ layer in a typical planar heterojunction device with a structure of Au/Spiro-OMeTAD/MAPbI₃/SnO₂/ITO, as shown in the cross-sectional scanning electron microscopy (SEM) image displayed in Scheme 1.



Scheme 1 Schematic illustration of the preparation of the two types of planar devices of PSCs studied in this work (left), and cross-sectional SEM image for the representative device (right).

Fig. 1a compares the surface of the two bilayer ETL films using SEM. The surface of SnO_2 NPs deposited on the ZnO (N/A) layer is flat and smooth, and it has less distinct graininess as compared to that on the ZnO (A) layer. This is consistent with the surface morphology observed by atomic force microscopy (AFM), where SnO_2/ZnO (N/A) has lower roughness than SnO_2/ZnO (A) (Fig. 1b). We attribute this result to the roughness of the underlying ZnO layer, where the ZnO is granulated to form nanoparticles under thermal annealing, so the thickness of the ZnO layer also shrank from ~ 16 nm to ~ 5 nm, as measured by AFM (Fig. S1†). Thus, a SnO_2 layer with a smoother surface and lower defect density was generated on the ZnO (N/A) film. However, there was no significant difference in the electrical conductivity for the bilayer ETLs. The perovskite (MAPbI_3) films formed on the bilayer ETLs were characterized by SEM (Fig. 1c) and X-ray diffraction (XRD) (Fig. 1d). The morphology and the crystallinity of MAPbI_3 films on the two different ETLs were comparable, and a flat surface with an average grain size of 200–300 nm was observed, suggesting that the perovskite crystal growth on the bilayer ETL was not affected by the morphology of the bottom layer (ZnO). A comparison of the UV-Vis absorption spectra for the perovskite layers on different ETLs further

confirms that the quality of the top perovskite layer was comparable irrespective of thermal annealing of the ZnO layer (Fig. S2a†). In order to study the role of the bilayer ETLs on charge transfer/recombination dynamics, photoluminescence (PL) of MAPbI_3 films and their decay on the bilayer ETLs were studied. Fig. 1e compares the decay curves of time-resolved PL (TRPL) from MAPbI_3 films with and without the bilayer ETLs. The typical PL spectrum of the pristine MAPbI_3 was centered at 775 nm, and it was effectively quenched with the bilayer ETLs, as shown in Fig. S2b.† The TRPL was fitted with a bi-exponential decay function of time (t): $I(t) = A_1 \exp(-t/\tau_1) + A_2 \exp(-t/\tau_2)$, where τ_1 and τ_2 represent the fast and slow decay time constant, and the average lifetime $\tau_{\text{ave}} = (A_1\tau_1^2 + A_2\tau_2^2)/(A_1\tau_1 + A_2\tau_2)$.²⁸ The fast-decay component (τ_1) is assigned to trap-assisted non-radiative recombination at the interface, while the slow decay component (τ_2) is attributed to radiative recombination of free carriers, which is mainly associated with charge transfer across the interface.²⁹ As summarized in Table S1,† the PL lifetime of pristine MAPbI_3 ($\tau_{\text{ave}} = 457.09$ ns) was reduced to 160.30 and 157.30 ns in the presence of SnO_2/ZnO (N/A) and SnO_2/ZnO (A), indicating effective charge transfer from MAPbI_3 to the bilayer ETLs. It is noted that the ratio of A_1/A_2 for SnO_2/ZnO (N/A) (0.67)

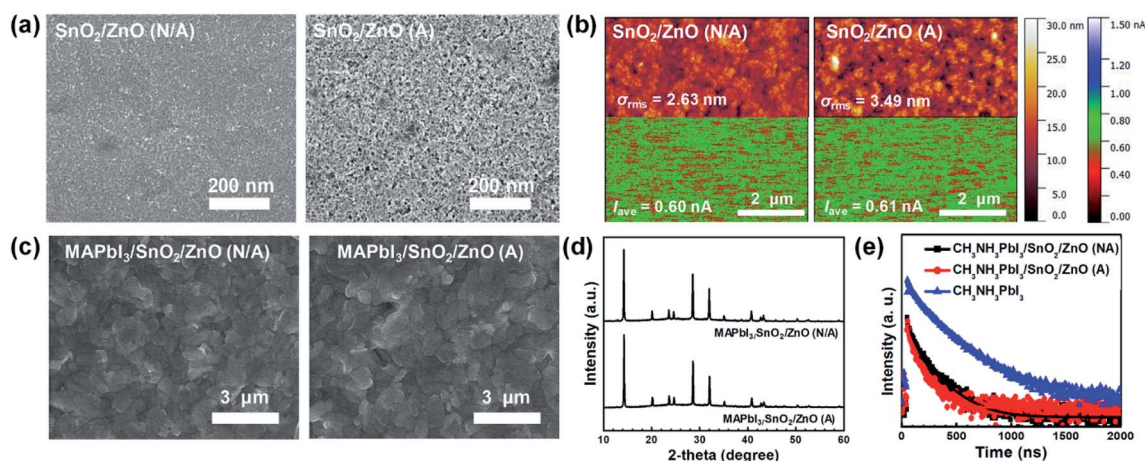


Fig. 1 SEM images (a) and AFM images (b) for SnO_2/ZnO (N/A) and SnO_2/ZnO (A) films. SEM images (c), X-ray diffractograms (d), and TRPL traces (e) of MAPbI_3 on SnO_2/ZnO (N/A) and SnO_2/ZnO (A) films.

is lower than that of SnO_2/ZnO (A) (0.85), which also suggests suppressed charge recombination at the interface of perovskite/ SnO_2/ZnO (N/A).³⁰

To evaluate the photovoltaic performance of the bilayer ETL-based PSCs, devices with a planar heterojunction structure were fabricated, as described in the Experimental. The current density–voltage (J – V) curves of the devices are shown in Fig. 2a, and the corresponding parameters are summarized in Table 1. The representative PCE of the SnO_2/ZnO (A)-based device is 17.34% with a V_{OC} of 1.10 V, a J_{SC} of 21.30 mA cm^{-2} , and a FF of 0.74. In the case of SnO_2/ZnO (N/A), the device achieved a higher PCE of 20.43% with a V_{OC} of 1.20 V, J_{SC} of 22.10 mA cm^{-2} , and a fill factor (FF) of 0.77. The control device based on a single ETL of SnO_2 exhibited a PCE of 16.66% with a V_{OC} of 1.09 V, J_{SC} of 21.90 mA cm^{-2} , and a fill factor (FF) of 0.69 (Fig. S3†). It is obvious that the improved PCE of the device with the optimized bilayer ETL is mainly attributed to the increased V_{OC} , and the probable underlying mechanisms will be discussed later. The stabilized power outputs (SPOs) for the PSCs were 20.42 and 17.23 mW cm^{-2} for the SnO_2/ZnO (N/A) and SnO_2/ZnO (A)-based devices under illumination of 100 mW cm^{-2} , respectively, which were consistent with PCEs from density–voltage (J – V) measurements (inset of Fig. 2a). The external quantum efficiency (EQE) spectra of the two devices are shown in Fig. 2b. The integration of the EQE spectrum with the AM 1.5G solar spectrum produced a photocurrent that is well matched with the J_{SC} derived from the J – V curve. Here the device with SnO_2/ZnO (N/A) exhibits higher photon-to-current conversion efficiency than that of SnO_2/ZnO (A) in the range of 500–750 nm, indicating

that enhanced carrier transfer/collection efficiency for the bilayer ETL with a non-annealed ZnO layer. This result is reproducible as presented in the histogram of PCE distribution from >15 individual devices fabricated with the bilayer ETLs, which verifies the feasibility of the bilayer ETLs, especially for SnO_2/ZnO (N/A), in realizing high-performance MAPbI₃-based PSCs (Fig. 2c).

As pointed out, the main reason for high PCEs of PSCs with the bilayer ETLs lies in the enhanced V_{OC} . The highest V_{OC} for the SnO_2/ZnO (A)-based devices is 1.10 V (1.06 V on average), while it is substantially increased to 1.20 V (1.17 V on average) with the SnO_2/ZnO (N/A) as an ETL (Fig. 2d). Importantly, these values are close to the SQL of V_{OC} for the single junction cell of MAPbI₃ under AM 1.5G, as illustrated in Fig. 2e.³¹ On the basis of the thermodynamic limit of V_{OC} , the J – V characteristic in the dark can be expressed by eqn (1), where J_0 is the saturated dark current density, q is the elementary charge, n is the diode ideality factor, k is Boltzmann's constant, T is temperature, R_s is the series resistance, R_{SH} is the shunt resistance, and J_{ph} is the photocurrent density.

$$J(V) = J_0 \left\{ \exp \left[\frac{q(V - R_s AJ)}{nkT} \right] - 1 \right\} + \frac{V - R_s AJ}{R_{\text{SH}} A} - J_{\text{ph}} \quad (1)$$

Under dark conditions, the photocurrent density should be zero and thus equal to J_{SC} . J_0 can be determined from the intercept at zero voltage of the linear regression from the semi-logarithmic J – V plot in the region close to the diode turn-on voltage³² (Fig. S4† and Table 1). For PSCs with the bilayer ETLs, J_0 was estimated to be 7.42×10^{-11} and $2.00 \times 10^{-9} \text{ mA}$

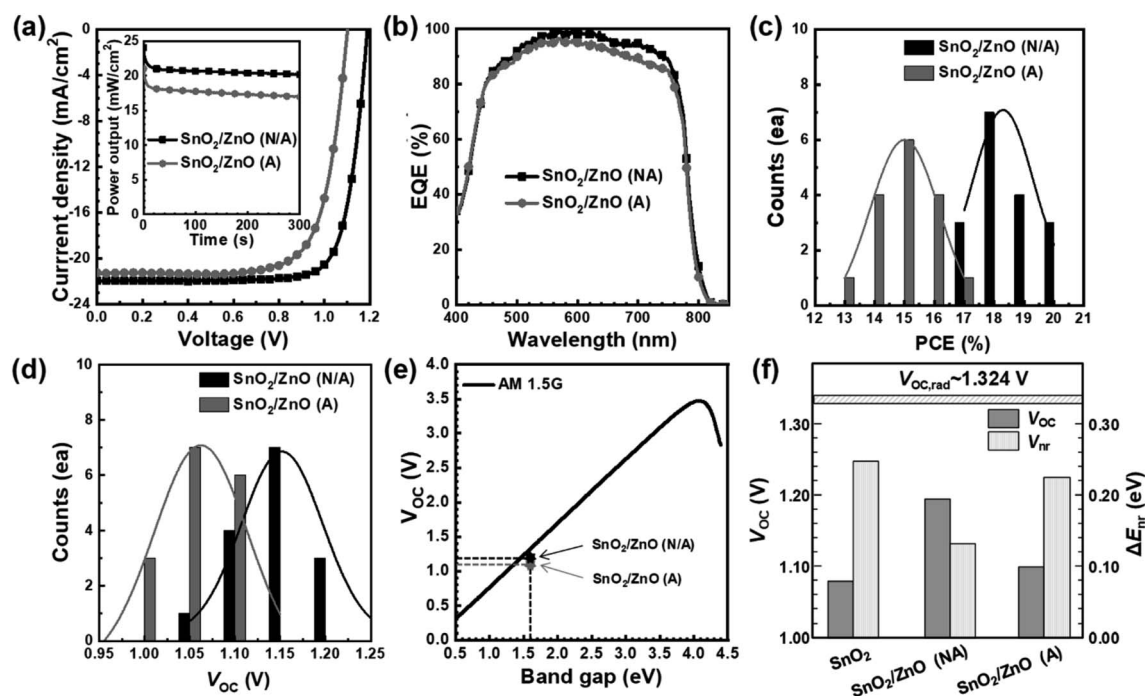


Fig. 2 J – V curves (a), EQE spectra (b), histogram of PCEs (c), and histogram of V_{OC} s (d) of the bilayer ETL-based PSCs fabricated in this work. The comparison for champion values of V_{OC} achieved in this work to the SQL (e), and corresponding non-radiative energy losses in the bilayer ETL-based PSCs (f). Inset of (a) shows SPO for 300 s under 1 sun illumination (100 mW cm^{-2}).

Table 1 Device parameters including photovoltaic parameters for the three PSCs with ETLs under 1 sun conditions (AM 1.5G, 100 mW cm⁻²)

ETL	V_{OC}^a [V]	J_{SC}^a [mA cm ⁻²]	FF ^a	PCE ^a [%]	J_{SC}^b [mA cm ⁻²]	n	J_0 [mA cm ⁻²]	$V_{OC,cal}$ [V]	V_{TFL} [V]	N_t
SnO ₂	1.09 (1.05)	21.90 (21.44)	0.69 (0.68)	16.66 (15.40)	21.85	2.24	9.20×10^{-8}	1.11	1.03	6.80×10^{15}
SnO ₂ /ZnO (N/A)	1.20 (1.17)	22.10 (21.76)	0.77 (0.75)	20.43 (19.26)	22.07	1.76	7.42×10^{-11}	1.21	0.81	5.35×10^{15}
SnO ₂ /ZnO (A)	1.10 (1.06)	21.40 (21.28)	0.74 (0.73)	17.34 (16.57)	21.45	1.92	2.00×10^{-9}	1.14	0.97	6.41×10^{15}

^a Average values in parentheses. ^b Integrated values from EQE spectra.

cm⁻² for SnO₂/ZnO (N/A) and SnO₂/ZnO (A), respectively, which are much smaller than that of SnO₂ (9.20×10^{-8} mA cm⁻²). Assuming that the R_{SH} is sufficiently higher than R_s in the device, eqn (1) can be described as eqn (2).³³

$$V_{OC} = \frac{nkT}{q} \ln\left(\frac{J_{SC}}{J_0} + 1\right) \quad (2)$$

For the bilayer ETLs, the calculated V_{OC} s were 1.21 and 1.14 V for the devices with SnO₂/ZnO (N/A) and SnO₂/ZnO (A), respectively, which are consistent to the realistic V_{OC} values measured during the J - V measurements under 1 sun irradiation. In spite of the J_{SC} of a typical PSC exceeding 20 mA cm⁻², J_0 , which is dependent on the degree of charge recombination, may vary by several orders of magnitude. The V_{OC} is also proportional to n , which is also related to the charge recombination in the cell. Thus, such high J_0 and n values in SnO₂ and

SnO₂/ZnO (A)-based devices imply un-optimized interfacial characteristics with high leakage current and significant carrier recombination in the device.³⁴ The energy loss (E_{loss}), which is described as E_{loss} (eV) = $E_g - qV_{OC}$, where q is the electron charge, is 0.38 and 0.48 eV for using SnO₂/ZnO (A) and SnO₂/ZnO (N/A) as ETLs, respectively, which are lower than that of the single ETL of SnO₂ (0.49 eV). For the E_{loss} in solar cells, more quantified analysis based on the balance theory provides more detailed E_{loss} that can be divided into three contributions ($E_{loss} = \Delta E_{SQ} + \Delta E_{rad} + \Delta E_{nr}$), where $\Delta E_{SQ} = E_g - qV_{OC,SQ}$; $\Delta E_{rad} = qV_{OC,SQ} - qV_{OC,rad}$; and $\Delta E_{nr} = qV_{OC,rad} - qV_{OC}$; $V_{OC,SQ}$ is V_{OC} in the Shockley-Queisser limit, and $V_{OC,rad}$ is V_{OC} in the radiative limit (Fig. S5†).^{35–37} Assuming that the radiative limit of V_{OC} ($V_{OC,rad}$) is ~ 1.324 V for a single-junction device of MAPbI₃ as reported elsewhere, the non-radiative energy loss (ΔE_{nr}) for the bilayer ETL-based devices was 0.124 and 0.224 eV for SnO₂/ZnO (N/A) and SnO₂/ZnO (A), respectively.³⁸ Apparently, the SnO₂/

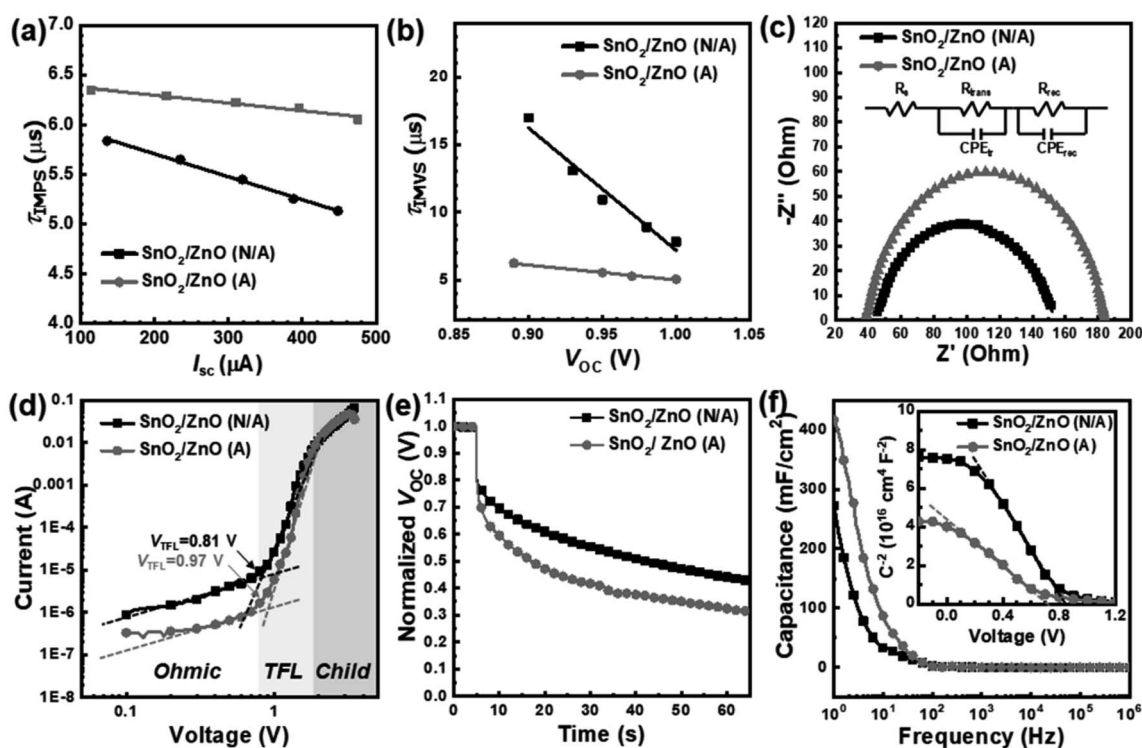


Fig. 3 Transit time constants (a), recombination lifetimes (b), Nyquist plots (c), dark J - V curves of the electron-only devices with the V_{TFL} kink points (d), OCVD curves (e), and capacitance analysis (f) for devices with the bilayer ETLs. Insets of (c) and (f) are the equivalent circuit for fitting and C^{-2} - V curves, respectively.

ZnO (N/A)-based device exhibited much reduced ΔE_{nr} as compared to SnO_2/ZnO (A), which indicates suppressed non-radiative recombination at the interface of perovskite/cathode in the presence of SnO_2/ZnO (N/A), and thus it boosted V_{OC} to 1.20 V for the MAPbI_3 -based single junction device (Fig. 3f).

To further study the charge carrier dynamics correlated with the non-radiative recombination at the interface, intensity-modulated photocurrent/photovoltage spectroscopy (IMPS/IMVS) was performed for the devices (Fig. 3a and b). In high-frequency light, the change in voltage or current is negligible because the cell does not have enough time to react, while the reaction time is long enough at low frequency. Thus, the mean transit time (τ_t) of photo-injected carriers and the time constant for electron-hole recombination (τ_r) could be analyzed by varying the light intensity.³⁹ The plots of τ_t versus J_{SC} show that the transit time constants are comparable in the two devices under varied light intensity, which indicates comparable electronic transport properties of the bilayer ETLs regardless of the bottom ZnO layer for the devices. This could be ascribed to the almost identical perovskite morphology as well as electrical conductivity of SnO_2/ZnO (N/A) and SnO_2/ZnO (A), which played similar roles as electron extraction/transport pathways to the cathode. In contrast, the device of SnO_2/ZnO (N/A) exhibited elongated τ_r as compared to the SnO_2/ZnO (A)-based device under varied light intensity (Fig. 3b). The longer recombination time constant implies a reduced mean rate for charge recombination at the interface between the perovskite and ETL in the device, which is consistent with the very low level dark current from the device of SnO_2/ZnO (N/A), as discussed above. Electrochemical impedance spectroscopy (EIS) was also conducted to further analyze details of charge transport resistance in the device. Fig. 3c presents Nyquist plots and the corresponding equivalent circuit model studied in this work. In a typical Nyquist plot of the planar heterojunction device, the high-frequency region represents the carrier-transport process with elements of the chemical capacitance (C_{trans}) and resistance (R_{trans}) in charge transport, while the low-frequency region represents the recombination process with a combination of recombination chemical capacitance (C_{rec}) and resistance (R_{rec}). As listed in Table S2,[†] the SnO_2/ZnO (A)-based device has larger R_{trans} and smaller R_{rec} values than the SnO_2/ZnO (N/A)-based one. Thus, it is suggested that the recombination process could be effectively suppressed as ZnO (N/A) was implanted in the bilayer ETL. To further gain insight into the trap density associated with interfaces in the device, we studied the space-charge limited current (SCLC) model by adopting the electron-only devices based on the bilayer ETLs. Fig. 3d shows their J - V curves. Under dark conditions, the dependence of J on V^n can be divided into three regions: ohmic region ($n = 1$), trap-filled limit (TFL) region ($n > 2$), and Child's region ($n = 2$); the transition between the ohmic and TFL regions is known as trap-filled limit voltage (V_{TFL}) according to the following equation (eqn (3)), where e is the elementary charge, ϵ_0 and ϵ are the permittivity of free space and the dielectric constant of the perovskite (32 for MAPbI_3), N_t is the trapped density of the thin film, and d is the thickness of the perovskite films.⁴⁰

$$V_{TFL} = \frac{eN_t d^2}{2\epsilon\epsilon_0 q} \quad (3)$$

The lower value of V_{TFL} in the SnO_2/ZnO (N/A)-based device further confirms the limited trap-state density at the interface of the PSC as compared to the SnO_2/ZnO (A)-based one (Table 1). It is noted here that the single ETL of SnO_2 exhibited the highest values of V_{TFL} and trap density as compared to the bilayer ETLs (Fig. S6[†]). With the reduced trap-state density, the V_{OC} decay (OCVD) for PSCs is thus elongated with the bilayer ETL of SnO_2/ZnO (N/A), which verifies the lowest charge recombination rate and the longest carrier lifetime, consistent with the results obtained from the TRPL, IMPS/IMVS, and EIS studies as discussed above. The capacitance characteristics of PSCs with the bilayer ETLs were also investigated. Fig. 3f shows frequency dependent capacitance under white light illumination. When SnO_2/ZnO (N/A) is used as an ETL, the capacitance at low frequency is lower than that with SnO_2/ZnO (A). The voltage-dependent capacitance is also shown in the inset of Fig. 3f. Given that the photo-generated charge carrier concentration at the perovskite/ETL interface is inversely proportional to the slope of the linear regime of the Mott-Schottky plot with an assumption of the same dielectric constant for the two devices, a steeper slope of the SnO_2/ZnO (N/A)-based device implies the reduced charge accumulation at the interface in the device, which is in agreement with the observations of suppressed non-radiative recombination at the interface of the perovskite and ETL as discussed above. All these results verify that the device with a bilayer ETL of SnO_2/ZnO (N/A) has a much longer carrier lifetime and lower interface recombination rate than that of SnO_2/ZnO (A), which is beneficial for increasing V_{OC} .⁴¹

In order to investigate the mechanism behind the reduced non-radiative recombination, photoelectron spectroscopy including X-ray photoelectron spectroscopy (XPS) and ultraviolet photoelectron spectroscopy (UPS) were conducted on the bilayer ETL. Fig. 4a shows distinct XPS peaks for O 1s and Sn 3d, which are attributed to the top SnO_2 layer of the bilayer ETLs. The asymmetric O 1s peak with lower binding energy (ca. 528 eV) can be assigned to O atoms in a metal-oxide lattice, and the other peak, at 530 eV, corresponds to an oxygen-deficient component or hydroxyl radicals.⁴² Given that electron-deficient components such as zinc hydroxide are a big part of ZnO (N/A) (Fig. S7[†]), the down-shift of O 1s in the bilayer ETL can be attributed to a decreased oxygen-deficient component arising from the ZnO (A) bottom layer. The binding energies for Sn 3p_{3/2} and Sn 3p_{5/2} peaks were also shifted from 493.1 to 492.7 eV and 484.8 to 484.3 eV, respectively, in the case of SnO_2/ZnO (N/A), and a similar binding energy shift was observed in Zn 2p (Fig. 4b). Given that the single SnO_2 layer exhibits almost the same binding energy as the SnO_2/ZnO (A), the up-shift in SnO_2/ZnO (N/A) can be ascribed to the oxide deficiency due to the lower valence state of Zn (2+) than Sn (4+). The variation in the electronic structure at the interface of SnO_2 and ZnO with respect to thermal annealing may influence the Fermi level for the bilayer ETLs. UPS spectra were recorded to investigate the energy levels of

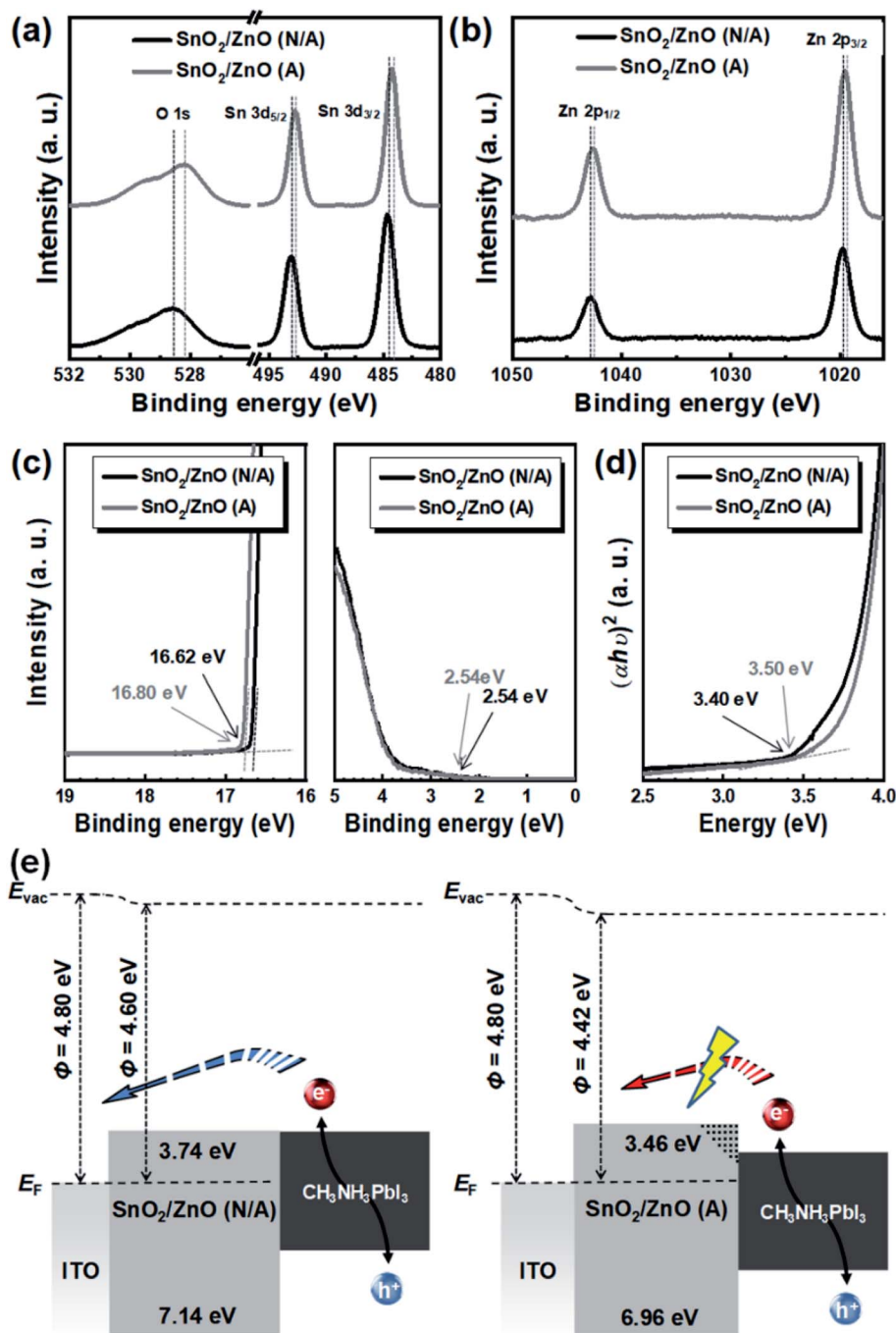


Fig. 4 XPS core level spectra for O 1s and Sn 3d (a), and Zn 2p (b), UPS cut-off edge and valence band (c), and Tauc plots for SnO₂/ZnO films (d). Schematic diagrams of band alignment and charge recombination at the interface between ITO and the MAPbI₃ layer (e).

the bilayer ETLs (Fig. 4c). The Fermi level (E_F) of SnO₂/ZnO (N/A) and SnO₂/ZnO (A) films was found to be -4.60 and -4.42 eV, respectively, from the cut-off binding energy ($E_{\text{cut-off}}$). The valence band maxima (E_{VB}) of the ETLs were found to be -6.82 (SnO₂/ZnO (N/A)) and -6.64 eV (SnO₂/ZnO (A)) with respect to the vacuum level, using the equation $E_{\text{VB}} = E_F - E_{\text{F,edge}}$. The conduction band minima (E_{CB}) of the bilayer ETLs were calculated to be -3.72 and -3.46 eV for SnO₂/ZnO (N/A) and SnO₂/ZnO (A), respectively, using the equation $E_{\text{CB}} = E_{\text{VB}} + E_g$, where the band gap (E_g) for the two films was obtained

from Tauc plots (Fig. 4d). The corresponding energy level alignment of the interfaces between the cathode and MAPbI₃ layer with respect to the bilayer ETLs is illustrated in Fig. 4e. Assuming that the conduction band of the CH₃NH₃PbI₃ film is -3.8 eV, SnO₂/ZnO (N/A) forms appropriate E_{CB} matching with the perovskite layer, while the steep downward shift of the Fermi level in SnO₂/ZnO (A) seems incompatible with the conduction band of the perovskite. This would be the main reason for the energy loss in the bilayer ETL with ZnO (N/A), which is beneficial for improving V_{OC} of the PSCs.

The most significant benefit of the bilayer ETL is the reduced non-radiative E_{loss} to achieve high V_{OC} under solar radiation. The low E_{loss} is crucial to retain its original V_{OC} in dim light such as the indoor environment because the impact of trap-assisted recombination is significant to limited charge carriers under low incident power of light sources.⁴³ In this regard, the photovoltaic performance of PSCs with the bilayer ETLs was examined under irradiation from white light-emitting diodes (LEDs) (6500 K). The power densities of the LED light used in this work were 156.1 and 309.8 $\mu\text{W cm}^{-2}$ for 500 and 1000 lux, respectively, from integration of spectral power density measured using a spectral light meter (Fig. S8†). Fig. 5a and b show J - V curves for the devices under LED light sources, and the photovoltaic parameters are listed in Table 2. The PSCs based on a single ETL of SnO_2 have maximum power outputs of 27.3 and 58.1 $\mu\text{W cm}^{-2}$ under 500 and 1000 lux, respectively, corresponding to PCEs of 17.5 and 18.8%, respectively. In the case of the bilayer ETLs, the maximum power outputs were substantially increased to 50.0 and 111.2 $\mu\text{W cm}^{-2}$ by using SnO_2/ZnO (N/A), and 49.0 and 107.9 $\mu\text{W cm}^{-2}$ by using SnO_2/ZnO (A) under 500 and 1000 lux, respectively, which correspond to PCEs up to 35.9 and 34.9% for SnO_2/ZnO (N/A) and SnO_2/ZnO (A)-based PSCs, respectively. Encouragingly, the devices with the bilayer ETLs retained higher V_{OC} of 0.98 and 0.95 V with SnO_2/ZnO (N/A) and SnO_2/ZnO (A), respectively, as compared to that of SnO_2 (0.75 V), which yields high PCEs under the LED light source. The steady power output of PSCs with the bilayer ETLs is stable for 300 s, and the SnO_2/ZnO (N/A)-based device delivered a stabilized power density of 115.3 $\mu\text{W cm}^{-2}$ under 1000 lux, corresponding to a PCE of 37.2% (Fig. 5c). It is noted

that this is a record efficiency for MAPbI_3 -based PSCs in the indoor environment (Table S3†). Fig. 5d displays the photon flux spectrum and integral current density of the LED light source with an intensity of 1000 lux. Based on the EQE for the device with SnO_2/ZnO (N/A), the integrated current density was calculated to be 149 $\mu\text{A cm}^{-2}$ which is consistent with the values from J - V measurements. The excellent PCE of the bilayer ETL-based PSCs in the indoor environment is attributed to the enhanced V_{OC} at low irradiation intensity (Fig. 5e). Compared to the device with a single ETL of SnO_2 , much improved V_{OC} s were obtained in the case of the bilayer ETLs. In particular, the device with SnO_2/ZnO (N/A) exhibited higher V_{OC} than that of the SnO_2/ZnO (A) at varied intensity from 200 to 1000 lux, which is the main cause of the superior PCE. Therefore, the optimized bilayer ETLs play a critical role in realizing a high PCE in the indoor environment. We also examined the operational stability of the devices under ambient conditions (Fig. 5f). The solar cells with SnO_2/ZnO (N/A) exhibited stabilized power density >97.5 $\mu\text{W cm}^{-2}$ (PCE $\sim 31.5\%$) for >800 h under ambient conditions with continuous irradiation of LED light (1000 lux), which is superior stability as compared to those of the other ETLs. Fig. S10† shows repeated measurements of SPO of devices under the LED light source (1000 lux) in the ambient atmosphere. The SnO_2/ZnO (N/A)-based device showed highly stable power generation over 840 h while the other devices exhibited relatively unstable power generation in >100 h. Since it is generally believed that hydroxyls on the surface of metal oxides are detrimental to decomposition of perovskite, the lowest ratio of O in hydroxyls to O in SnO_2/ZnO (N/A) (0.45) to the ratio for SnO_2/ZnO (A) (0.75) or single SnO_2 (0.81) can account for the

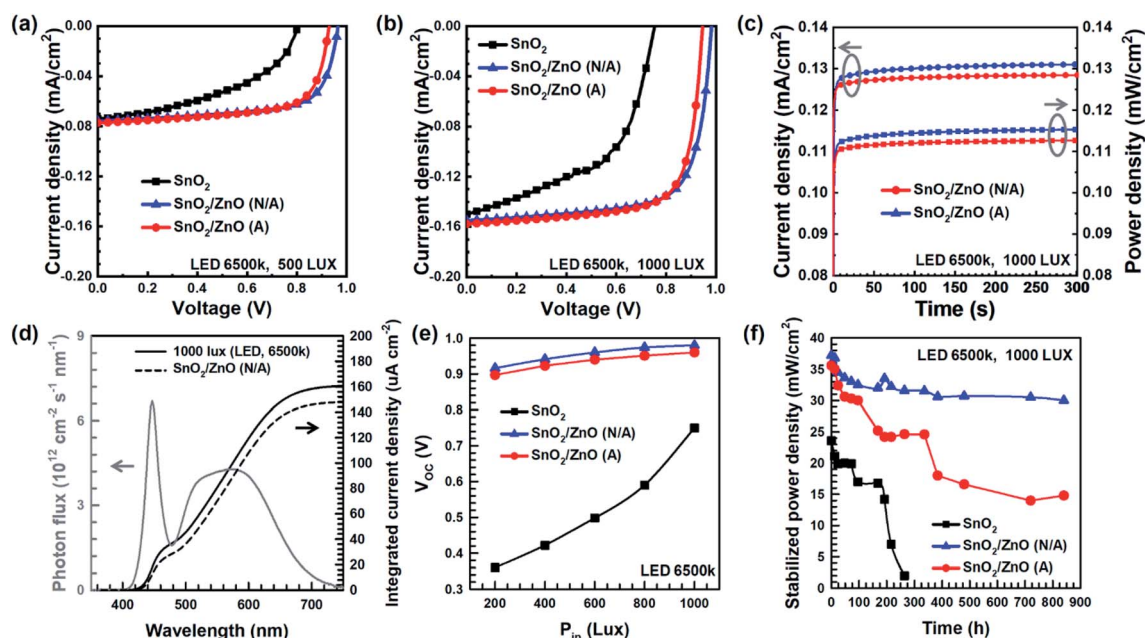


Fig. 5 J - V curves of the PSCs with different ETLs under a white LED light source (6500 K) with intensities of 500 lux (a) and 1000 lux (b), steady current density generation and corresponding power output as a function of time held at a bias of 0.88 V (c), photon flux and integrated current density spectra over the white LED (1000 lux) with the device incorporating the bilayer ETL (d), V_{OC} change of different ETL-based PSCs as a function of light intensity from the white LED light source (e), and PCE decay under ambient conditions and continuous irradiation from the white LED light source (f).

Table 2 Photovoltaic parameters for the three PSCs under a white LED light source (6500 K)

Light intensity [lux/ $\mu\text{W cm}^{-2}$]	ETL	V_{OC} [V]	J_{SC} [$\mu\text{A cm}^{-2}$]	FF	Power density [$\mu\text{W cm}^{-2}$]	PCE ^a [%]	SPO [$\mu\text{W cm}^{-2}$]	PCE ^b [%]
500/156.1	SnO ₂	0.80	74.0	0.46	27.3	17.5	—	—
	SnO ₂ /ZnO (N/A)	0.97	77.1	0.70	52.1	33.4	—	—
	SnO ₂ /ZnO (A)	0.93	77.0	0.71	50.4	32.3	—	—
1000/309.8	SnO ₂	0.89	149.9	0.52	76.4	24.7	62.6	20.2
	SnO ₂ /ZnO (N/A)	0.98	157.6	0.72	111.2	35.9	115.2	37.2
	SnO ₂ /ZnO (A)	0.95	157.7	0.72	107.9	34.8	113.0	36.5

^a PCEs from J - V measurements. ^b PCEs from SPO measurements.

better long-term stability of the device of SnO₂/ZnO (N/A) in comparison with the other ETLs^{44,45} (Fig. S10†). Therefore, it is demonstrated that PSCs with bilayer ETLs have great advantages in practical applications due to their excellent PCEs and stability under indoor illumination conditions.

4. Conclusions

In summary, we presented a new design of a bilayer ETL based on SnO₂ and ZnO for achieving high photovoltaic performance in MAPbI₃-based PSCs. It was found that thermal annealing modulates the Fermi level of the bottom ZnO layer in the bilayer ETL, and thus the bilayer ETL made of SnO₂/ZnO (N/A) enhanced the superior film quality, suppressed trap density, and reduced charge recombination at the interface of ETL/perovskite of the resulting devices. One of the primary advantages of the bilayer ETL outlined in this work is the low non-radiative E_{loss} , which yielded a PCE of 20.43% with a high V_{OC} up to 1.20 V in MAPbI₃-based single junction PSCs in the outdoor environment (1 sun conditions). Taking advantage of the low E_{loss} at high intensity illumination, the bilayer ETL retained a high V_{OC} of 0.98 V of the devices in the indoor environment (LED light, 1000 lux), realizing an excellent PCE of 37.2% with excellent ambient stability, outperforming the other reported perovskite photovoltaic technologies in indoor applications. This design strategy for ideal interfacial contact suggests promising prospects of the perovskite photovoltaic technologies and will significantly promote the development of high-performance PSCs with efficient power outputs in outdoor/indoor environments.

Conflicts of interest

The authors declare no competing financial interest.

Acknowledgements

This research was supported by the Basic Science Research Program through a National Research Foundation of Korea (NRF) grant funded by the Ministry of Science, ICT & Future Planning (Grant Number: 2017R1C1B2009691). This work was supported by a National Research Foundation of Korea (NRF)

grant funded by the Korean government (MSIT) (No. 2017H1D8A2031138).

References

- 1 N. G. Park, Perovskite Solar Cells: An Emerging Photovoltaic Technology, *Mater. Today*, 2015, **18**, 65–72.
- 2 N. G. Park, Research Direction toward Scalable, Stable, and High Efficiency Perovskite Solar Cells, *Adv. Energy Mater.*, 2020, **10**, 1903106.
- 3 M. A. Green, A. Ho-Baillie and H. J. Snaith, The Emergence of Perovskite Solar Cells, *Nat. Photonics*, 2014, **8**, 506–514.
- 4 C. Wehrenfennig, G. E. Eperon, M. B. Johnston, H. J. Snaith and L. M. Herz, High Charge Carrier Mobilities and Lifetimes in Organolead Trihalide Perovskites, *Adv. Mater.*, 2014, **26**, 1584–1589.
- 5 J. Qi, H. Xiong, G. Wang, H. Xie, W. Jia, Q. Zhang, Y. Li and H. Wang, High-performance solar cells with induced crystallization of perovskite by an evenly distributed CdSe quantum dots seed-mediated underlayer, *J. Power Sources*, 2018, **376**, 46–54.
- 6 B. Wang, J. Iocozzia, M. Zhang, M. Ye, S. Yan, H. Jin, S. Wang, Z. Zou and Z. Lin, The charge carrier dynamics, efficiency and stability of two-dimensional material-based perovskite solar cells, *Chem. Soc. Rev.*, 2019, **48**, 4854–4891.
- 7 J. Qi, L. Li, H. Xiong, A. C. Wang, C. Hou, Q. Zhang, Y. Li and H. Wang, Highly efficient walking perovskite solar cells based on thermomechanical polymer films, *J. Mater. Chem. A*, 2019, **7**, 26154–26161.
- 8 J. Qi, H. Xiong, C. Hou, Q. Zhang, Y. Li and H. Wang, A kirigami-inspired island-chain design for wearable moistureproof perovskite solar cells with high stretchability and performance stability, *Nanoscale*, 2020, **12**, 3646–3656.
- 9 M. He, B. Li, X. Cui, B. Jiang, Y. He, Y. Chen, D. O'Neil, P. Szymanski, M. A. El-sayed, J. Huang and Z. Lin, Meniscus-assisted solution printing of large-grained perovskite films for high-efficiency solar cells, *Nat. Commun.*, 2017, **8**, 16045.
- 10 NREL Best Research-Cell Efficiency Chart, <https://www.nrel.gov/pv/cell-efficiency.html>.

- 11 C. Wehrenfennig, G. E. Eperon, M. B. Johnston, H. J. Snaith and L. M. Herz, Fundamental Efficiency Limit of Lead Iodide Perovskite Solar Cells, *J. Phys. Chem. Lett.*, 2018, **9**, 1703–1711.
- 12 S. Rühle, Tabulated Values of the Shockley–Queisser Limit for Single Junction Solar Cells, *Sol. Energy*, 2016, **130**, 139.
- 13 N.-G. Park and H. Segawa, Research Direction toward Theoretical Efficiency in Perovskite Solar Cells, *ACS Photonics*, 2018, **5**(8), 2970–2977.
- 14 T. Kirchartz, High Open-Circuit Voltages in Lead-Halide Perovskite Solar Cells: Experiment, Theory and Open Questions, *Philos. Trans. R. Soc., A*, 2019, **377**, 20180286.
- 15 J. P. Correa-Baena, M. Saliba, T. Buonassisi, M. Gratzel, A. Abate, W. Tress and A. Hagfeldt, Promises and Challenges of Perovskite Solar Cells, *Science*, 2017, **358**, 739–744.
- 16 J. J. Yoo, S. Wieghold, M. C. Sponseller, M. R. Chua, S. N. Bertram, N. T. P. Hartono, J. S. Tresback, E. C. Hansen, J.-P. Correa-Baena, V. Bulović, T. Buonassisi, S. S. Shin and M. G. Bawendi, An Interface Stabilized Perovskite Solar Cell With High Stabilized Efficiency and Low Voltage Loss, *Energy Environ. Sci.*, 2019, **12**, 2192–2199.
- 17 M. Stolterfoht, C. M. Wolff, J. A. Márquez, S. Zhang, C. J. Hages, D. Rothhardt, S. Albrecht, P. L. Burn, P. Meredith, T. Unold and D. Neher, Visualization and Suppression of Interfacial Recombination for High-Efficiency Large-Area Pin Perovskite Solar Cells, *Nat. Energy*, 2018, **3**, 847–854.
- 18 C. M. Wolff, F. Zu, A. Paulke, L. P. Toro, N. Koch and D. Neher, Reduced Interface-Mediated Recombination for High Open-Circuit Voltages in $\text{CH}_3\text{NH}_3\text{PbI}_3$ Solar Cells, *Adv. Mater.*, 2017, **29**, 1700159.
- 19 Q. Wang, Q. Dong, T. Li, A. Gruverman and J. Huang, Thin Insulating Tunneling Contacts for Efficient and Water-Resistant Perovskite Solar Cells, *Adv. Mater.*, 2016, **28**, 6734–6739.
- 20 P. Caprioglio, F. Zu, C. M. Wolff, J. A. Márquez Prieto, M. Stolterfoht, P. Becker, N. Koch, T. Unold, B. Rech, S. Albrecht and D. Neher, High open circuit voltages in pin-type perovskite solar cells through strontium addition, *Sustainable Energy Fuels*, 2019, **3**, 550–563.
- 21 S. Yang, J. Dai, Z. Yu, Y. Shao, Y. Zhou, X. Xiao, X. C. Zeng and J. Huang, Tailoring Passivation Molecular Structures for Extremely Small Open-Circuit Voltage Loss in Perovskite Solar Cells, *J. Am. Chem. Soc.*, 2019, **141**, 5781.
- 22 A.-N. Cho and N.-G. Park, Impact of Interfacial Layers in Perovskite Solar Cells, *ChemSusChem*, 2017, **10**, 3687–3704.
- 23 J. Pospisil, O. Zmeskal, S. Nespurek, J. Krajcovic, M. Weiter and A. Kovalenko, Density of Bulk Trap States of Hybrid Lead Halide Perovskite Single Crystals: Temperature Modulated Space-Charge-Limited-Currents, *Sci. Rep.*, 2019, **9**, 3332.
- 24 M. Zhang, M. Ye, W. Wang, C. Ma, S. Wang, Q. Liu, T. Lian, J. Huang and Z. Lin, Synergistic Cascade Carrier Extraction via Dual Interfacial Positioning of Ambipolar Black Phosphorene for High-Efficiency Perovskite Solar Cells, *Adv. Mater.*, 2020, **32**, 2000999.
- 25 J. Dou, Y. Zhang, Q. Wang, A. Abate, Y. Li and M. Wei, Highly Efficient Zn_2SnO_4 Perovskite Solar Cells Through Band Alignment Engineering, *Chem. Commun.*, 2019, **55**, 14673–143676.
- 26 J. Lu, G. Yang and G. Fang, Perovskite Solar Cells Based on Low-Temperature Processed Indium Oxide Electron Selective Layers, *ACS Appl. Mater. Interfaces*, 2016, **8**, 8460–8466.
- 27 S. S. Shin, E. J. Yeom, W. S. Yang, S. Hur, M. G. Kim, J. Im, J. Seo, J. H. Noh and S. I. Seok, Colloidally Prepared La-Doped BaSnO_3 Electrodes for Efficient, Photostable Perovskite Solar Cells Highly Efficient Zn_2SnO_4 Perovskite Solar Cells Through Band Alignment Engineering, *Science*, 2017, **356**, 167–171.
- 28 F. Wei, B. Jiao, H. Dong, J. Xu, T. Lei, J. Zhang, Y. Yu, L. Ma, D. Wang, J. Chen, X. Hou and Z. Wu, Bifunctional π -Conjugated Ligand Assisted Stable and Efficient Perovskite Solar Cell Fabrication via Interfacial Stitching, *J. Mater. Chem. A*, 2019, **7**, 16533–16540.
- 29 M. Zhang, X. Cui, Y. Wang, B. Wang, M. Ye, W. Wang, C. Ma and Z. Lin, Simple Route to Interconnected, Hierarchically Structured, Porous Zn_2SnO_4 Nanospheres as Electron Transport Layer for Efficient Perovskite Solar Cells, *Nano Energy*, 2020, **74**, 104620.
- 30 Z. Wu, M. Jiang, Z. Liu, A. Jamshaid, L. K. Ono and Y. Qi, Highly Efficient Perovskite Solar Cells Enabled by Multiple Ligand Passivation, *Adv. Energy Mater.*, 2020, **10**, 1903696.
- 31 T. C.-J. Yang, P. Fiala, Q. Jeangros and C. Ballif, *Joule*, 2018, **2**, 1421–1436.
- 32 C. Li, Z. S. Wang, H. L. Zhu, D. Zhang, J. Q. Cheng, H. Lin, D. Ouyang and W. C. H. Choy, Thermionic Emission-Based Interconnecting Layer Featuring Solvent Resistance for Monolithic Tandem Solar Cells with Solution-Processed Perovskites, *Adv. Energy Mater.*, 2018, **8**, 1801954.
- 33 Z. Liu, L. Krückemeier, B. Krogmeier, B. Klingebiel, J. A. Márquez, S. Levchenko and S. Levchenko, *ACS Energy Lett.*, 2019, **4**, 110–117.
- 34 C. Wang, C. Xiao, Y. Yu, D. Zhao, R. A. Awni, C. R. Grice, K. Ghimire, D. Constantinou, W. Liao, A. J. Cimaroli, P. Liu, J. Chen, N. J. Podraza, C.-S. Jiang, M. M. Al-Jassim, X. Zhao and Y. Yan, Reducing Saturation-Current Density to Realize High Efficiency Low-Bandgap Mixed Tin-Lead Halide Perovskite Solar Cells, *Adv. Energy Mater.*, 2017, **7**, 17000414.
- 35 U. Rau, B. Blank, T. C. M. Müller and T. Kirchartz, Efficiency Potential of Photovoltaic Materials and Devices Unveiled by Detailed-Balance Analysis, *Phys. Rev. Appl.*, 2017, **7**, 044016.
- 36 U. Rau, Reciprocity Relation Between Photovoltaic Quantum Efficiency And Electroluminescent Emission Of Solar Cells, *Phys. Rev. B: Condens. Matter Mater. Phys.*, 2007, **76**, 085303.
- 37 S. Liu, J. Yuan, W. Deng, M. Luo, Y. Xie, Q. Liang, Y. Zou, Z. He, H. Wu and Y. Cao, High-Efficiency Organic Solar Cells With Low Non-Radiative Recombination Loss and Low Energetic Disorder, *Nat. Photonics*, 2020, **14**, 300.
- 38 W. Tress, N. Marinova, O. Inganäs, M. K. Nazeeruddin, S. M. Zakeeruddin and M. Grätzel, Predicting the Open-Circuit Voltage of $\text{CH}_3\text{NH}_3\text{PbI}_3$ Perovskite Solar Cells Using

- Electroluminescence and Photovoltaic Quantum Efficiency Spectra: The Role of Radiative and Non-Radiative Recombination, *Adv. Energy Mater.*, 2015, 5, 1400812.
- 39 H.-C. Kwon, W. Yang, D. Lee, J. Ahn, E. Lee, S. Ma, K. Kim, S.-C. Yun and J. Moon, Investigating Recombination and Charge Carrier Dynamics in a One-Dimensional Nanopillared Perovskite Absorber, *ACS Nano*, 2018, 12, 4233–4245.
 - 40 M. I. Saidaminov, A. L. Abdelhady, B. Murali, E. Alarousu, V. M. Burlakov, W. Peng, I. Dursun, L. Wang, Y. He, G. Maculan, A. Goriely, T. Wu, O. F. Mohammed and O. M. Bakr, High-quality Bulk Hybrid Perovskite Single Crystals Within Minutes By Inverse Temperature Crystallization, *Nat. Commun.*, 2015, 6, 7586.
 - 41 J. Ma, G. Yang, M. Qin, X. Zheng, H. Lei, C. Chen, Z. Chen, Y. Guo, H. Han, X. Zhao and G. Fang, MgO Nanoparticle Modified Anode for Highly Efficient SnO_2 -Based Planar Perovskite Solar Cells, *Adv. Sci.*, 2017, 4, 1700031.
 - 42 S. W. Knipe, J. R. Mycroft, A. R. Pratt, H. W. Nesbitt and G. M. Bancroft, X-ray Photoelectron Spectroscopic Study Of Water Adsorption On Iron Sulphide Minerals, *Geochim. Cosmochim. Acta*, 1995, 59, 1079–1090.
 - 43 S. W. Knipe, J. R. Mycroft, A. R. Pratt, H. W. Nesbitt and G. M. Bancroft, Tailoring Triple-Anion Perovskite Material for Indoor Light Harvesting with Restrained Halide Segregation and Record High Efficiency Beyond 36%, *Adv. Energy Mater.*, 2019, 9, 1901980.
 - 44 Y. Cheng, Q. D. Yang, J. Xiao, Q. Xue, H. W. Li, Z. Guan, H. L. Yip and S. W. Tsang, Decomposition of Organometal Halide Perovskite Films on Zinc Oxide Nanoparticles, *ACS Appl. Mater. Interfaces*, 2015, 7, 19986–19993.
 - 45 J. Yang, B. D. Siempelkamp, E. Mosconi, F. D. Angelis and T. L. Kelly, Origin of the Thermal Instability in $\text{CH}_3\text{NH}_3\text{PbI}_3$ Thin Films Deposited on ZnO, *Chem. Mater.*, 2015, 27, 4229–4236.